Study on the evolution of discharge times on electrical contact properties of Ag-V$_2$AlC composite material

Xiaochen Huang[1,2]*, Jinlong Ge[1,2], Zijue Zhou[3]*, Junyang Hong[1], Dabao Zhang[1] and Tianle Xu[1]

[1]School of Material and Chemical Engineering, Bengbu University, Bengbu, Anhui, China, [2]Engineering Technology Research Center of Silicon-Based Materials, Bengbu University, Anhui, China, [3]School of Chemistry and Materials Engineering, Huainan Normal University, Huainan, China

An Ag-20 vol.% V$_2$AlC composite material was prepared using the spark plasma sintering method. The influence of the number of arc discharge on the electrical contact performance of Ag-V$_2$AlC composites was systematically investigated. For the first time, we observed that the arc ablation mechanism evolves with increasing discharge cycles. During single arc ablation, the arc preferentially discharges the Ag phase owing to its lower work function. This process creates a relatively flat ablation region where the V$_2$AlC reinforcement and Ag matrix remain distinct. The V$_2$AlC phase acts as a pinning agent within the Ag matrix, effectively suppressing material splatter. After 10 discharge cycles, the ablation edge of the Ag-V$_2$AlC material develops a mountain-like morphology. This structure prevents material splashing and results in no pores or splatter on the surface. The phase boundary between V$_2$AlC and Ag becomes less distinct, while the breakdown current stabilizes between 19.9 A and 24.1 A. Concurrently, the breakdown strength fluctuates within 4.3×10^6 V/m to 8.2×10^6 V/m. Following 100 discharge cycles, the Ag and V$_2$AlC phases are no longer distinguishable in the ablation area. Micro-protrusions form in the central ablation region, enhancing the local electric field and ultimately reducing the breakdown strength. As discharges increase further, the concentration of low-work-function oxides (V$_2$O$_5$, Al$_2$O$_3$, and Ag$_2$O) rises. These oxides dominate the arc discharge process, further diminishing the breakdown strength. Consequently, the breakdown strength exhibits a three-stage decreasing trend. Although the ablation area expands with discharge cycles, oxide formation increases the molten pool viscosity, preventing significant splatter at the ablation edge. These findings provide a theoretical foundation for designing novel electrical contact materials with enhanced performance.

KEYWORDS

Ag-V2AlC, Ag-MAX, electrical contact material, breakdown strength, arc ablation

1 Background

With the rapid advancement of modern technology, electrical contact materials face increasingly stringent performance demands in fields such as power electronics, communications, circuit breakers, and aerospace. These materials are critical components in electrical systems, enabling both energy and signal transmission. Their performance

directly governs the reliability, stability, and lifespan of electrical equipment (Han et al., 2024; Nian et al., 2023). Silver (Ag) has been widely adopted as a baseline electrical contact material due to its exceptional electrical and thermal conductivity, oxidation resistance, and ease of processing. However, pure silver exhibits limitations, including low hardness, poor arc corrosion resistance, and vulnerability to sulfidation in sulfur-rich environments. These drawbacks hinder its broader application in electrical contacts (Sone and Takagi, 1990). To overcome the weaknesses of pure silver, researchers have developed silver-based composites, primarily categorized into two groups: AgCu (Mousavi and Pourabdoli, 2022), AgNi (Li H. et al., 2024) and AgW (Zhao et al., 2023; Kesim et al., 2018); and silver metal oxides (AgSnO$_2$ (Nie et al., 2024; Zhao et al., 2024), AgCuO (Wang H. et al., 2023), and AgZnO (Guzmán et al., 2023).

Ag-based composites reinforced with MAX phases ($M_{n+1}AX_n$) have emerged as promising alternatives to conventional toxic Ag/CdO electrical contact materials. These composites uniquely combine superior electrical, thermal, and mechanical properties (Sun, 2011; Barsoum, 2000). MAX phases, such as Ti$_3$AlC$_2$, Ti$_2$SnC, and Ti$_3$SiC$_2$, exhibit exceptional electrical conductivity, thermal conductivity, and thermal stability. These characteristics make them excellent candidates for reinforcing Ag matrices (Wu et al., 2025; Ding et al., 2022; Wang et al., 2020; Wang D. et al., 2019; Wu et al., 2024). For example, Ag-Ti$_3$AlC$_2$ composites demonstrate performance comparable to Ag/CdO in accelerated arc tests, attributed to the superior wettability between Ag and MAX phases. Furthermore, Ag-MAX composites retain high electrical conductivity and hardness, benefiting from the metallic-ceramic duality intrinsic to MAX phases. Thus, Ag-MAX composites represent a transformative advancement in electrical contact materials. They integrate environmental safety, exceptional arc erosion resistance, and tunable microstructural adaptability. Future research should prioritize optimizing the composition and processing of Ag-MAX composites to fully realize their potential in next-generation electrical systems. Here, V$_2$AlC was chosen due to its exceptional electrical resistivity (0.25 μΩ m) (Sun, 2011), thermal conductivity (48 W·m^{-1}·K^{-1}) (Gong and Wang, 2025), and prior evidence of interfacial compatibility with Ag (Wang et al., 2024).

Ag-V$_2$AlC composites were prepared using a spark plasma sintering method (SPS). In the experimental setup, the Ag-V$_2$AlC composite served as the cathode, while a sharp-tipped tungsten (W) rod functioned as the anode. A voltage applied between the electrodes generated a strongly nonuniform electric field, facilitating arc formation. The initiation of the arc depends critically on the work function of the contact material, as well as its intrinsic properties and surface roughness. This study systematically investigates the effects of discharge cycles (1, 10, and 100 cycles) on the arc ablation mechanism of Ag-V$_2$AlC composites. Furthermore, it explores how ablation products and surface morphology influence the breakdown strength and molten pool characteristics of the composites. Key findings elucidate the dynamic evolution of the arc ablation mechanism in Ag-V$_2$AlC composites. These results are anticipated to advance the application of Ag-MAX composites in high-performance electrical contact materials, particularly in systems requiring enhanced arc resistance and controlled interfacial behavior.

TABLE 1 Lattice parameters of V$_2$AlC used in VASP.

Crystal axis length (Å)		Crystal axis length (°)	
a	2.91	α	90
b	2.91	β	90
c	13.65	γ	120

2 Materials and methods

2.1 Sample preparation

The V$_2$AlC material ((>98%, 200 mesh, Laizhou Kai Kai Ceramic Materials Co., Ltd.), with a volume fraction of 20%, and Ag powder (>99.8%, 200 mesh, Sinopharm Group Chemical Reagent Co.), with a volume fraction of 80%, were mechanically mixed for 2 h to achieve a homogeneous mixed powder. The Ag-V$_2$AlC composite was prepared by SPS furnace (SPS-3T-3-MIN, Shanghai Chenhua Science Technology Corp., Ltd.), which involved placing the mixed powder into a graphite mold after initial pressing on a tablet press. The preparation process included heating the mixture to 700°C at a rate of 100°C/min and maintaining this temperature for 10 min with 30 MPa pressure. Following this, the samples were taken out for grinding and polishing after cooling with the furnace until the roughness of the sample surface was lower than 0.5 μm. The composition of the sintered samples was analyzed using an X-ray diffractometer (XRD, SmartLabSE, Japan), while density was assessed using Archimedes' method, and microhardness was measured with a microhardness tester (YZHV-IZP, Shanghai Aolong Xingdi Testing Instrument Co., Ltd.).

2.2 Calculation of the V$_2$AlC work function

The crystal structure information of V$_2$AlC materials is shown in Table 1. First-principles calculations of spin polarization were conducted using the Perdew-Burke-Ernzerhof (PBE) exchange-correlation functional within the VASP program, employing the projected augmented wave (PAW) method along with the corresponding pseudopotentials. The convergence criteria for energy and force were set to 10^{-5} eV and 0.01 eV/Å, respectively, with an energy cutoff of 600 eV established for the plane wave basis set. A K-point mesh of 12 × 12 × 1 was utilized. To prevent interactions between the model and its periodic images, a vacuum layer of 15 Å was incorporated in the z-direction of the (0001)-cut structure, and dipole correction in the z-direction was applied in the calculations.

2.3 Arc erosion test

The Ag-V$_2$AlC composite material was subjected to an arc ablation experiment using a self-made arc ablation device, with an acrylic plate employed to create a closed environment. Within this enclosed space, the Ag-V$_2$AlC composite material served as

the cathode, while a W rod was utilized as the anode, and the front end of the anode was machined into the shape of a circular arc with a diameter of 2 mm. After fixing the initial positions of the cathode and anode, a voltage of 7 kV was applied across the two electrodes. Once the voltage stabilized at 7 kV, the cathode was gradually brought closer to the anode. An arc was generated before the two electrodes made contact, resulting in the ablation of the surface of the Ag-V$_2$AlC composite material. Subsequently, the cathode was returned to its initial position, and a voltage of 7 kV was applied again to initiate a second arc ablation. This procedure was repeated for multiple arc ablation experiments. During each discharge event, a digital oscilloscope was employed to capture the current value of the arc and the duration of arc combustion. Additionally, a stepper motor was utilized to measure the discharge distance between the two electrodes upon the cessation of a single discharge. The breakdown strength value for each discharge was calculated using Equation 1.

$$E = \frac{U}{d} \tag{1}$$

where E is breakdown strength (V/m), U is applied load(V), d is discharge distance between the two electrodes (m).

The surface of Ag-V$_2$AlC composite material after different discharge ablation was characterized by morphology and composition. Morphological analysis was conducted by a three-dimensional laser scanning morphology (3D LSCM, Keyence VK-X250, Keyence Corporation, Osaka, Japan) and a thermal field emission scanning electron micro oscope (TFE-SEM, ZEISS Gemini 500, Carl Zeiss AG, Oberkochen, Germany). The composition analysis was performed with a Raman spectrometer (Lab RAM-HR, HORIBA, Kyoto, Japan).

3 Results

3.1 Physical properties

Figure 1 presents the X-ray diffractogram (XRD) and mapping-scan analysis of the sintered Ag-V$_2$AlC composite. The XRD analysis confirms distinct peaks corresponding to Ag and V$_2$AlC, indicating the coexistence of both phases after sintering. This phase distribution aligns with the composition of the initial powder mixture. Figure 1b demonstrates a uniform dispersion of V$_2$AlC within the Ag matrix. The density of the Ag-V$_2$AlC composite, measured via the Archimedes' method, was 96.1%. Microhardness testing yielded three independent measurements, with corresponding micro-indentations shown in Figure 2. The diagonal lengths of the indentations are detailed in Table 2. The average microhardness value was determined as 82.6 HV.

3.2 Results of single arc ablation

The Ag-V$_2$AlC composite underwent single arc ablation at a loading voltage of 7 kV. The ablated surface morphology is shown in Figure 3. Figures 3a–c display color-mode 3D laser scanning microscope images of the composite. In Figure 3a, the ablation

center is demarcated by circle 1, while the heat-affected zone spans the area between circles 1 and 2. Magnified views of the ablation center are provided in Figures 3b, c. Notably, the ablation center exhibits a relatively flat morphology with no observable pits. A 3D topographic reconstruction of this region (Figure 3d) further confirms the absence of prominent pits or bulges across the ablated surface.
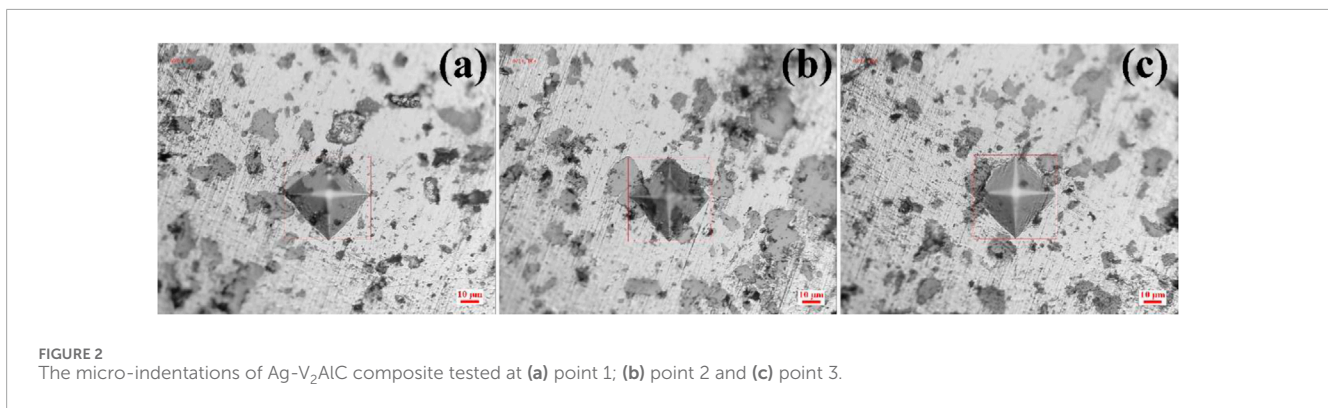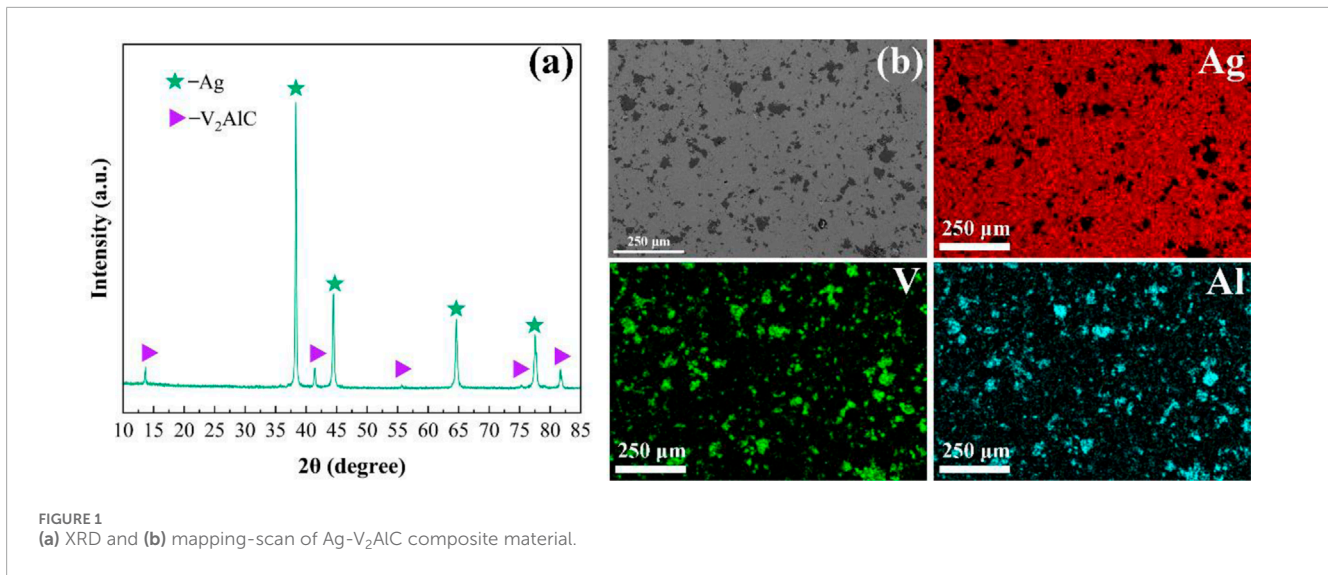
The surface morphology of the Ag-V$_2$AlC composite after single arc ablation was analyzed via scanning electron microscopy (SEM), as shown in Figure 4. Figure 4a provides an overview of the ablated surface, with magnified views of regions labeled Rectangles 1–3 displayed in Figures 4b–d, respectively. The ablation traces in Figure 4a show no prominent ablation features.

Figure 5 shows the results of mapping–scan analysis after one arc ablation. It can be seen that the V$_2$AlC phase is clearly visible and still retains the size and shape of the un-ablated one (Figure 1b). The V$_2$AlC reinforcing phase remains distinct within the Ag matrix. This is attributed to the lower melting point of Ag, which melts preferentially under electron bombardment. Additionally, the work function of Ag (4.26–4.47 eV (Yang, 1983; Michaelson, 1950)) is significantly lower than that of V$_2$AlC (6.4128 eV), causing the arc to discharge preferentially through the Ag phase. In Figure 4b, V$_2$AlC particles (highlighted by dashed circles) exhibit minimal ablation. Figures 4c, d reveal localized re-solidified molten material at the ablation edge (indicated by arrows), with no significant splattered particles. This suppression of splatter is attributed to the thermally stable V$_2$AlC phase, which pins the molten Ag flow and mitigates splashing—a mechanism previously observed in TiC-reinforced Cu composites (Xiao et al., 2007). Notably, the ablation behavior of Ag-V$_2$AlC contrasts sharply with other MAX-phase composites. Pure Ti$_3$AlC$_2$ and Cu-20 vol.% Ti$_3$AlC$_2$ composites ablated under identical conditions (7 kV) exhibit extensive pores and splattered particles (Huang et al., 2017; Huang et al., 2018). Ag-Ti$_3$SiC$_2$ composites show distinct craters, protrusions, and a larger ablation area compared to Ag-V$_2$AlC (Huang et al., 2020). These comparisons demonstrate the superior arc ablation resistance of Ag-V$_2$AlC composites, likely due to the synergistic effects of V$_2$AlC's high work function, thermal stability, and effective pinning of the Ag matrix.

Figure 6 shows the current-time curve of the Ag-V$_2$AlC composite during arc discharge. As the electrodes approach, air ionization triggers arc formation, causing the current to peak at the breakdown current (23.8 A). After a stable arc burning phase, the current decays to zero as the arc extinguishes. The total duration from arc initiation to extinction—termed the arcing time—is 31.7 ms. The breakdown strength, calculated from the peak voltage and electrode gap, is 7.9×10^6 V/m.

3.3 Results of ten arc ablations

Figure 7 illustrates the surface morphology of the Ag-V$_2$AlC composite after ten arc ablations. Similar to the single ablation case (Figure 3), Figure 7a shows distinct ablation center and edge regions. The ablation center region expands progressively, as detailed in Figures 7b, c. Figure 7b reveals protruding features (green arrows), while Figure 7c highlights overlapping ablation edges (green arrows) formed by repeated discharges.

FIGURE 1
(a) XRD and (b) mapping-scan of Ag-V$_2$AlC composite material.

FIGURE 2
The micro-indentations of Ag-V$_2$AlC composite tested at (a) point 1; (b) point 2 and (c) point 3.

TABLE 2 Indentation diagonal lengths of Ag-V$_2$AlC composite material.

Test point	d1 (µm)	d2 (µm)	d (µm)	Hardness (HV)
1	48.929	47.202	48.07	80.2
2	46.554	47.202	46.88	84.3
3	47.202	47.202	47.20	83.2

A 3D reconstruction of the surface (Figure 7d) demonstrates mountain range-like ablation edges (white circles) and pits (white arrows) formed by cumulative arc damage. Compared to the single ablation (Figure 3), the surface exhibits significantly greater degradation, including enlarged ablation zones, protrusions, and pits, underscoring the progressive deterioration under repeated arc exposure.

The surface morphology of the Ag-V$_2$AlC composite after ten arc ablation cycles is shown in Figure 8. Figure 8a displays the overall ablated region, with magnified views of Rectangles 1–3 provided in Figures 8b–d, respectively. Figure 8b highlights ablation edge structures (indicated by double arrows) formed by repeated arc exposure. A prominently raised feature, marked by an arrow in Figure 8c, aligns with the mountain-like morphology observed in Figure 7d. Additionally, Figure 8d reveals significant surface pores (arrows), indicative of progressive material degradation under cyclic ablation. Similar to the results of the face scan after one discharge in Figure 5, the V$_2$AlC phase is discernible in the region encased inside the ablation in Figure 9.

Figures 10a, b depict the breakdown current and breakdown strength of Ag-V$_2$AlC composites as functions of discharge cycles. The breakdown current fluctuates between 19.9 A and 24.1 A, while the breakdown strength ranges from 4.3×10^6 V/m to 8.2×10^6 V/m.

3.4 100 arc ablation results

Figure 11 illustrates the surface morphology of the Ag-V$_2$AlC composite after 100 arc ablations. The ablation region (Figure 11a) exhibits concentrated damage, with a mountain-like edge morphology (arrow in Figure 11b) resembling the features observed after 10 cycles (Figure 7d). Many protrusions are presented in the locally enlarged area in Figure 11b. Repeated ablations produce raised topographic profiles (Figure 11c), and the ablated
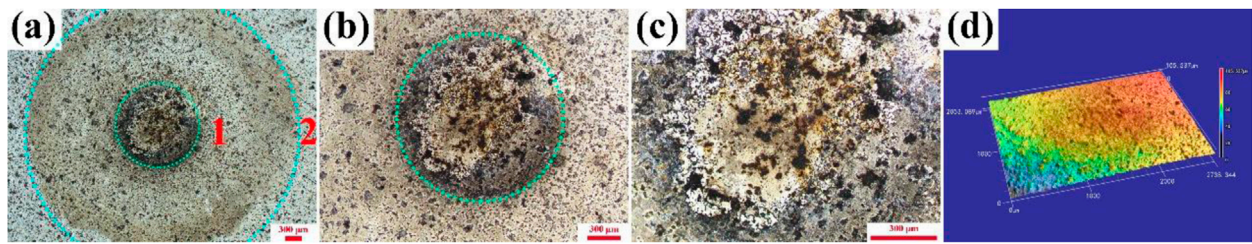
FIGURE 3
(a–c) Surface morphology of Ag-V$_2$AlC material after single arc ablation **(d)** 3D reconstruction of the surface of Ag-V$_2$AlC material after arc ablation.
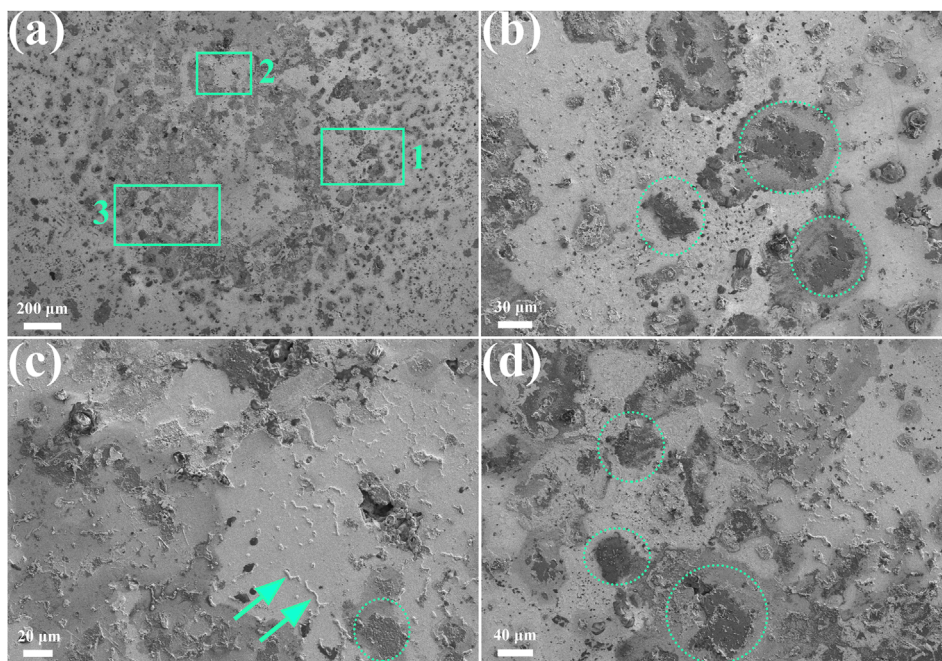

FIGURE 4
(a) Overall morphology of a single ablation **(b–d)** Local enlarged morphology corresponding to the rectangles 1, 2 and 3, respectively.

area expands significantly compared to the 10-cycle case (Figure 7a). 3D topographic analysis (Figure 11d) reveals a maximum height of 199.344 μm, far exceeding the 11.921 μm observed after 10 cycles. This height increase arises from the overlapping and stacking of ablation edges, which restrict molten pool expansion and amplify vertical growth. Notably, the Ag-V$_2$AlC composite demonstrates superior arc resistance compared to Ag-Ti$_3$SiC$_2$. Prior studies report that Ag-Ti$_3$SiC$_2$ exhibits a larger ablation area and more severe surface degradation under identical conditions (Huang et al., 2020).

Figure 12 presents the microscopic morphology of the Ag-V$_2$AlC composite after 100 arc ablations. Due to the ablation area exceeding the scanning electron microscope's field of view, Figure 12a captures only a partial region of the ablated surface. The magnified ablation edge in Figure 12b reveals a width of approximately 100 μm. The red arrows in Figure 12b indicate the micro protrusions formed after multiple ablations, with fine particles observed between the protrusions, as shown in the partially enlarged

view in Figure 12c. Figure 12d clearly demonstrates that the ablation edge bulges to a certain height, effectively preventing the outward spattering of the molten pool. Figure 12d demonstrates that the ablated edge bulges to a significant height, effectively suppressing molten pool splatter. Notably, unlike Ti$_3$AlC$_2$ (Huang et al., 2017), the Ag-V$_2$AlC surface shows no splattered particles at the ablation edge (Huang et al., 2020). Furthermore, after 100 cycles, the Ag-V$_2$AlC surface lacks substantial pores—a stark contrast to Cu-Ti$_3$AlC$_2$ and Ag-Ti$_3$SiC$_2$ composites, which exhibit extensive porosity under identical conditions (Huang et al., 2020; Huang et al., 2019b). Additionally, after 100 arc ablations, the surface does not exhibit the pores that were present after 10 arc ablations, potentially due to the molten pool filling the pores as it flows in all directions under the influence of the arc force. In Figure 13, the elements Ag, V, Al, C and O are basically spread over the ablated area without a clearly discernible V$_2$AlC phase similar to those in Figures 5, 9. This is because the surface oxides of Ag-V$_2$AlC composites increase after
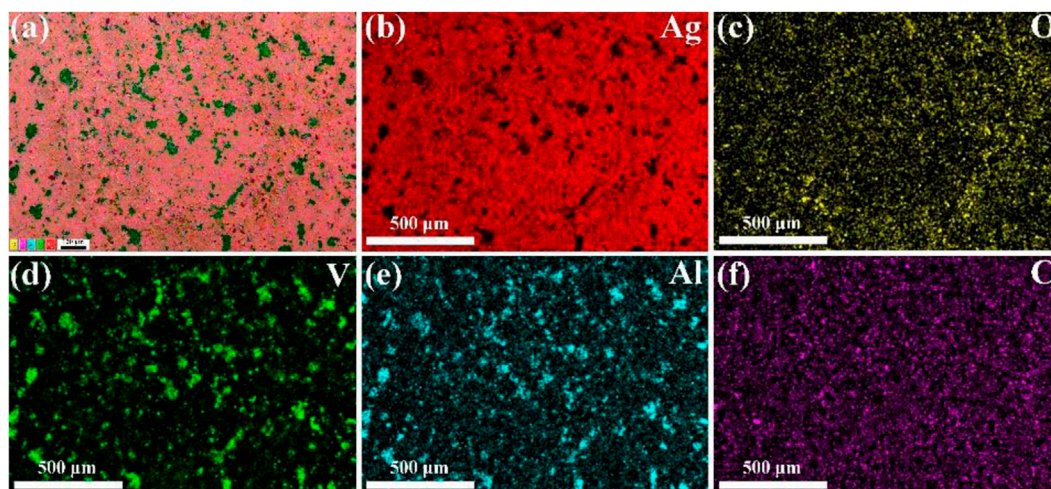
FIGURE 5
Mapping−scan results of Ag-V$_2$AlC composites after one arc ablation.
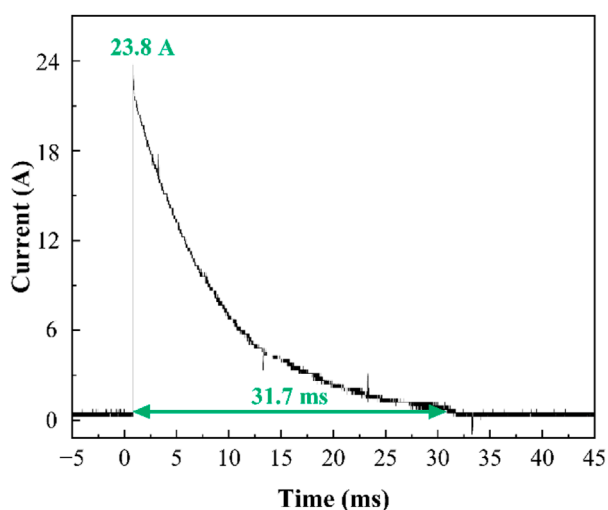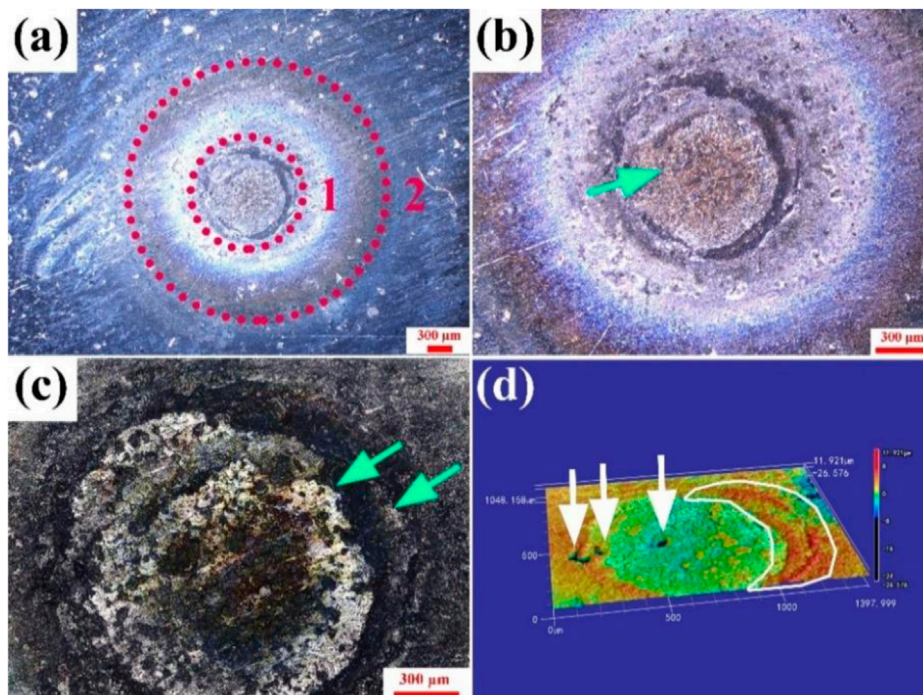

FIGURE 6
Curve of current-time of Ag-V$_2$AlC composite material.

several arc ablations, and at the same time, the molten pool is mixed together by repeated plasma force (as shown in Figure 15), which makes the Ag, V, Al, C and O elements uniformly distributed on the ablated surface.

Raman spectroscopy analysis of Ag-V$_2$AlC composites after varying arc discharge cycles is shown in Figure 14. Figures 14a, b correspond to single arc ablation, revealing characteristic peaks of V$_2$O$_5$ (229 cm^{-1}), Ag$_2$O (957 and 1,053 cm^{-1}), and Al$_2$O$_3$ (240 cm^{-1}) (X050043) (Baddour-Hadjean et al., 2012; Smirnov et al., 2018; Anjum et al., 2017; Martína et al., 2012). Similar oxide phases are observed after 10 and 100 arc ablations (Figures 14c, d), confirming persistent surface oxidation across all tested cycles. These results demonstrate that vanadium, silver, and aluminum oxides form during arc ablation, indicating decomposition and oxidation of the Ag-V$_2$AlC composite under repeated discharges.

This experiment was conducted in a confined air environment with a 7 kV voltage applied between the Ag-V$_2$AlC cathode (circular sheet) and a tungsten (W) anode (sharp-tipped rod), as shown in Figure 15. This configuration creates a strongly nonuniform electric field, ionizing air molecules to generate negative and positive ions. Charged particles accelerate toward the electrodes, triggering electron avalanches and forming a conductive plasma channel (positive streamer) across the gap (Huang et al., 2024), as shown in Figures 15c, d. High-velocity electrons bombard the Ag-V$_2$AlC composite surface, transferring energy to surface atoms. This energy induces localized melting (Figure 15e). In addition, plasma forces (both electromagnetic and thermodynamic) have a significant effect on the melt pool surface, as show in Figure 15d. Plasma forces are usually directed in the same direction as the arc current and are strongest in the center of the arc. This force pushes the molten material in the melting pool outward, causing craters to form on the ablated surface. As the number of discharges increases and the arc repeatedly acts on the surface of the material, plasma forces continue to act on the molten pool, pushing the molten material to diffuse outward and re-solidify. This repeated melting-diffusion-solidification process causes the pit area of the molten pool to gradually increase, as shown in Figures 15f, g. The plasma force is relatively weak at the edges of the molten pool, resulting in the buildup of molten material in the edge region. With the increase of the number of discharges, this stacking effect is gradually significant, forming a mountain range-like edge phase, as shown in Figure 15h. In addition, at the edge of the melt pool, the plasma force is relatively weak, and the molten material receives less thrust, and thus is more likely to stack up in the edge region. With the increase of the number of discharges, this stacking effect gradually accumulates, and finally a mountain range-like edge phase is formed, as shown in Figure 12d.

Meanwhile, some atoms gain sufficient energy to overcome the material's work function, escaping into the atmosphere and reacting with oxygen ions to form oxides (V$_2$O$_5$, Ag$_2$O, Al$_2$O$_3$). Studies confirm that oxide incorporation enhances matrix-reinforcement

FIGURE 7
(a–c) Surface morphology of Ag-V$_2$AlC material after ten arc ablations **(d)** 3D reconstruction of the surface of Ag-V$_2$AlC material after ten arc ablations.
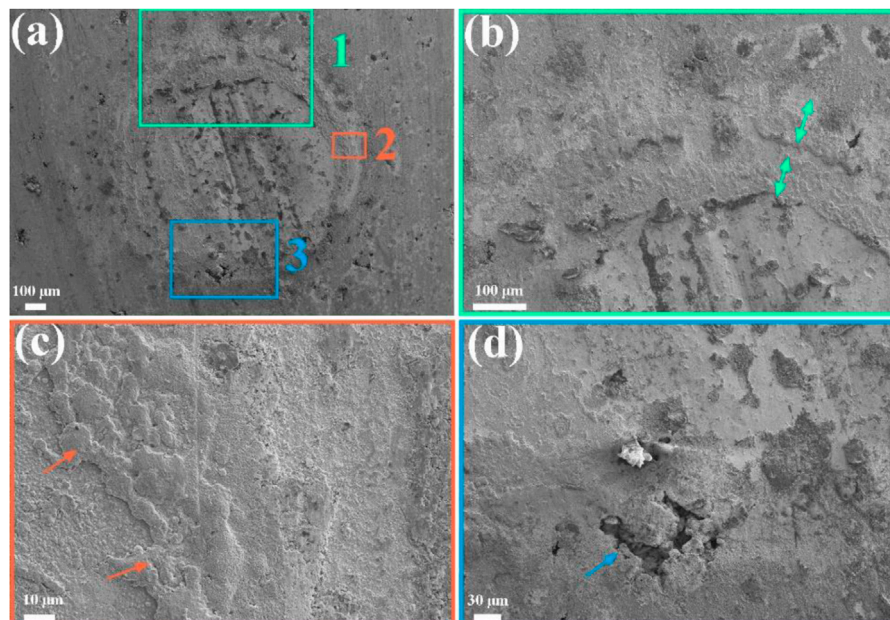
FIGURE 8
(a) Overall morphology of ten arc ablations **(b–d)** Local enlarged morphology corresponding to the rectangles 1, 2 and 3, respectively.

wettability (Li W-J. et al., 2024; Wang J. et al., 2019; Chen et al., 2021; Han et al., 2017; Wang J. et al., 2023; Wang et al., 2022), increasing molten pool viscosity and suppressing material splatter. The crystal structure of these oxides further governs interfacial

wettability (Ma et al., 2018). As shown in Figures 8, 12, the mountain-like morphology of ablation edges suggests that V$_2$O$_5$, Ag$_2$O, and Al$_2$O$_3$ formation promotes molten pool stabilization. This mechanism reduces splatter by increasing viscosity, a critical
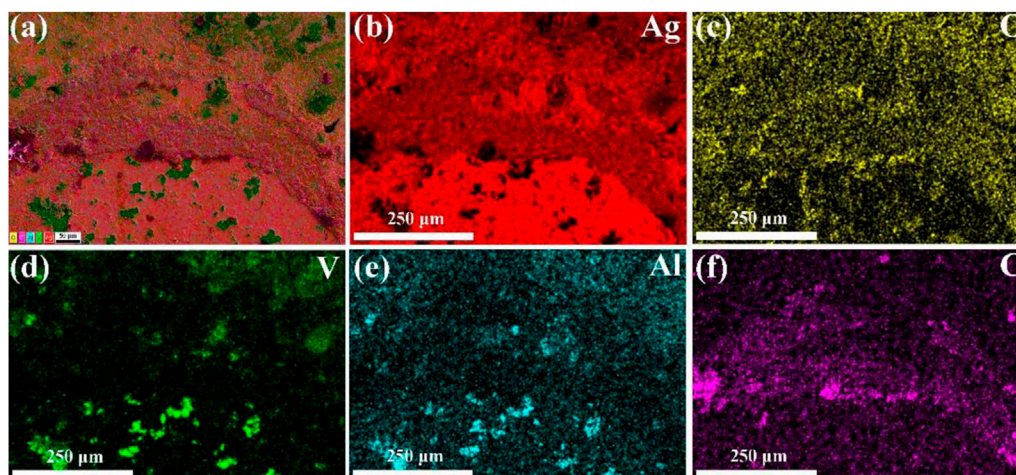
FIGURE 9
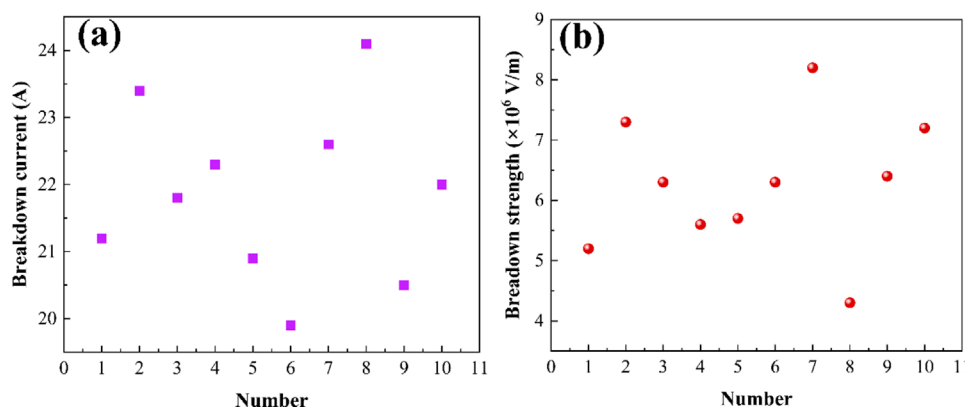Mapping−scan results of Ag-V$_2$AlC composites after ten arc ablations.

FIGURE 10
Scatter plots of **(a)** breakdown current and **(b)** breakdown strength with the number of discharges.

advantage over conventional composites (e.g., Ag/CdO) that lack such oxide-mediated dynamic control.

Scatter plots illustrating the variations in breakdown current and breakdown strength across 100 arc ablations are presented in Figure 16. As shown, the breakdown current fluctuates between 18.4 A and 34 A, with a primary concentration between 19 A and 27 A. Breakdown strength is a physical quantity used to assess the ease with which an electric arc can occur. The higher the breakdown strength, the less likely the arc will occur, and conversely, the lower the breakdown strength, the more likely the arc will occur. Notably, the breakdown strength, exhibiting a substantial range that fluctuates from 8.24×10^6 V/m to 1.68×10^6 V/m. The trend of breakdown strength depicted in Figure 16b can be categorized into three distinct stages, labeled as stages 1, 2, and 3. The first stage encompasses the 1st to 14th discharges, the second stage spans the 15th to 44th discharges, and the third stage covers the 45th–100th discharges.

(1) Stage I (1–14 discharges): air breakdown and oxide formation. Atmospheric ionization initiates due to cosmic radiation, generating weakly ionized gases with 500–1,000 charged particle pairs/cm^3. Under the applied electric field, these particles form a positive streamer, triggering arc discharge (Anjum et al., 2017). During this stage, the breakdown strength fluctuates between 8.24×10^6 V/m and 3.46×10^6 V/m (Figure 16b). The elevated initial breakdown strength is attributed to an adsorbed air layer on the cathode surface, which increases the effective work function of the Ag-V$_2$AlC composite (Beukema, 1980; Huang et al., 2019a). This air layer temporarily enhances dielectric resistance before progressive arc-induced oxidation dominates.

The breakdown strength magnitude depends on intrinsic material properties, including work function, thermal conductivity, and electrical conductivity (Dong et al., 2017). Jiang et al. found that the breakdown strength of Ag/SnO$_2$ material was correlated with the coating thickness (Jiang et al., 2012). Yang et al. observed the
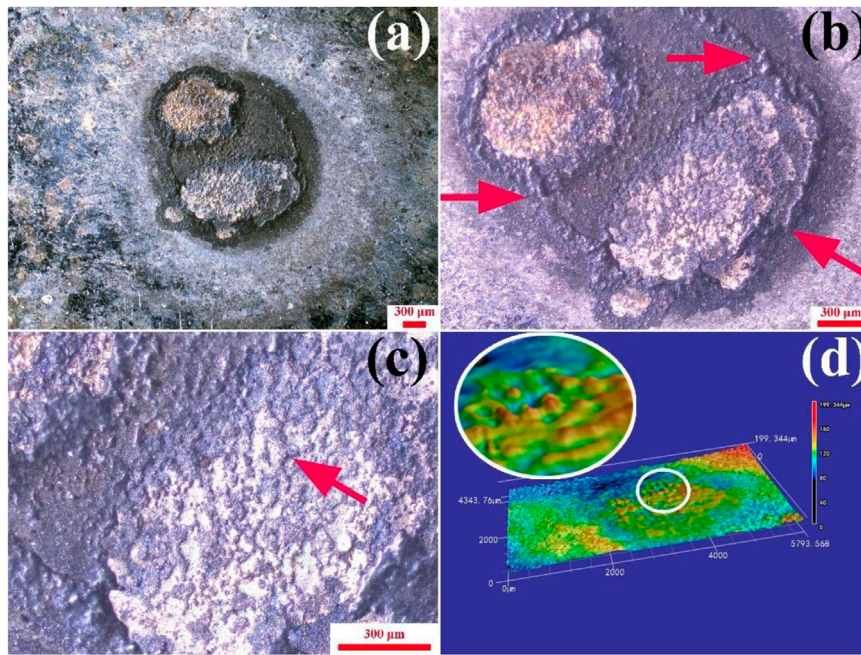
FIGURE 11
(a–c) Surface morphology of Ag-V$_2$AlC material after 100 arc ablations **(d)** 3D reconstruction of the surface of Ag-V$_2$AlC material after 100 arc ablations.
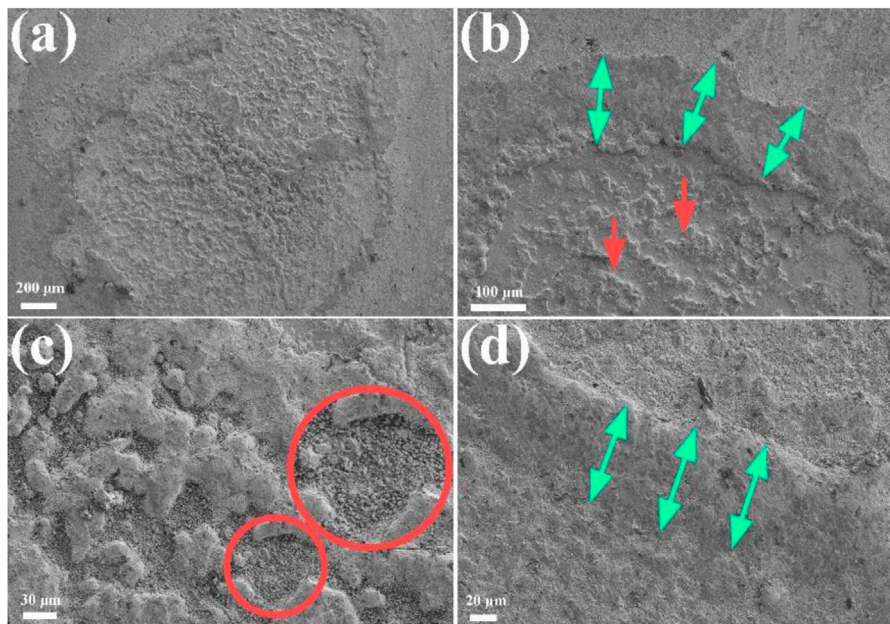
FIGURE 12
(a) Partial morphology of 100 arc ablations **(b–d)** Local enlarged morphology.

breakdown strength of CuW alloy with TiB$_2$ addition was higher (Yang et al., 2024). Ding et al. found that the breakdown strength of plasma sprayed Ag/(Sn$_{0.8}$La$_{0.2}$) layers tended to decrease with the increase of the number of discharges (Fu et al., 2012). Yang et al. found that the microstructure of WCu30 Alloy affected the magnitude of the breakdown strength (Xingang et al., 2015). Chen et al. found that

solid solution strengthening, fine grain strengthening and deformation strengthening can improve the breakdown strength of Cu-Cr-Zr alloys (Zhou et al., 2020). Zhu et al. found that the degradation of the electrical insulation properties may lead to a decrease in the electrical breakdown strength (Nie et al., 2023). Wang et al. claimed that the addition of appropriate amount of Al$_2$O$_3$ can improve the
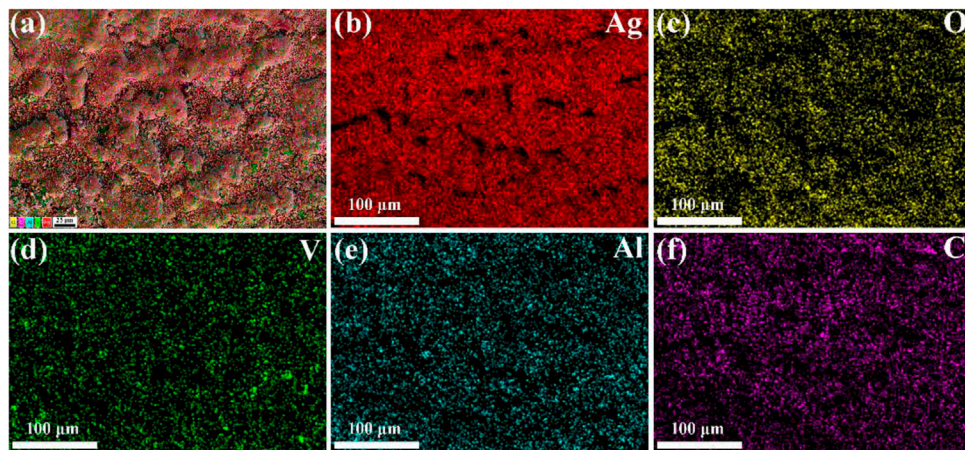
FIGURE 13
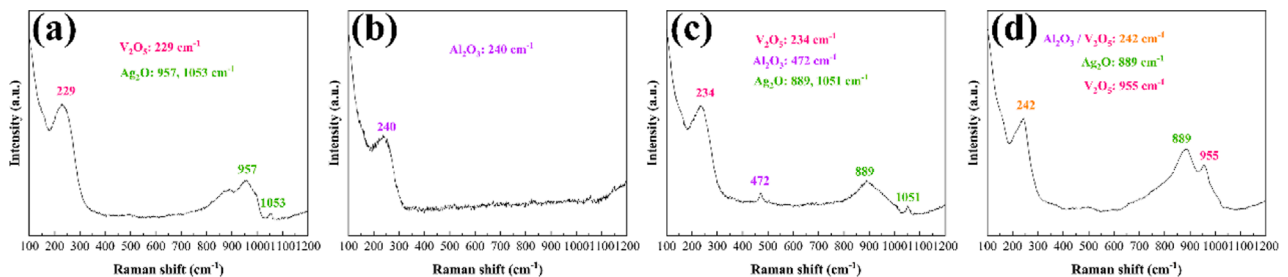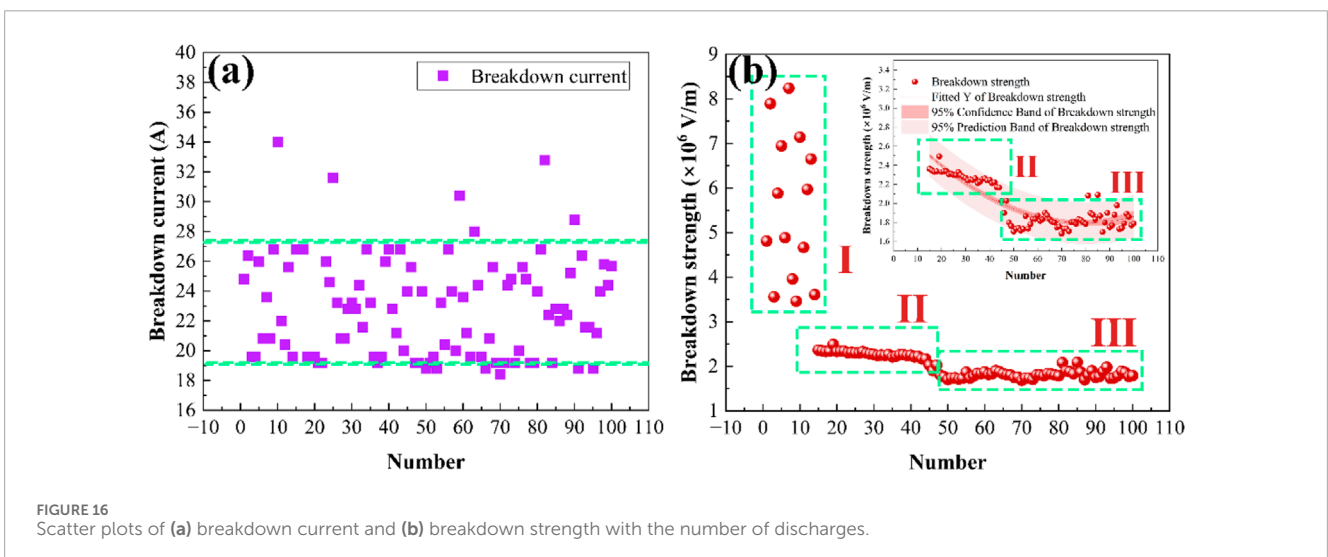Mapping−scan results of Ag-V$_2$AlC composites after 100 arc ablations.
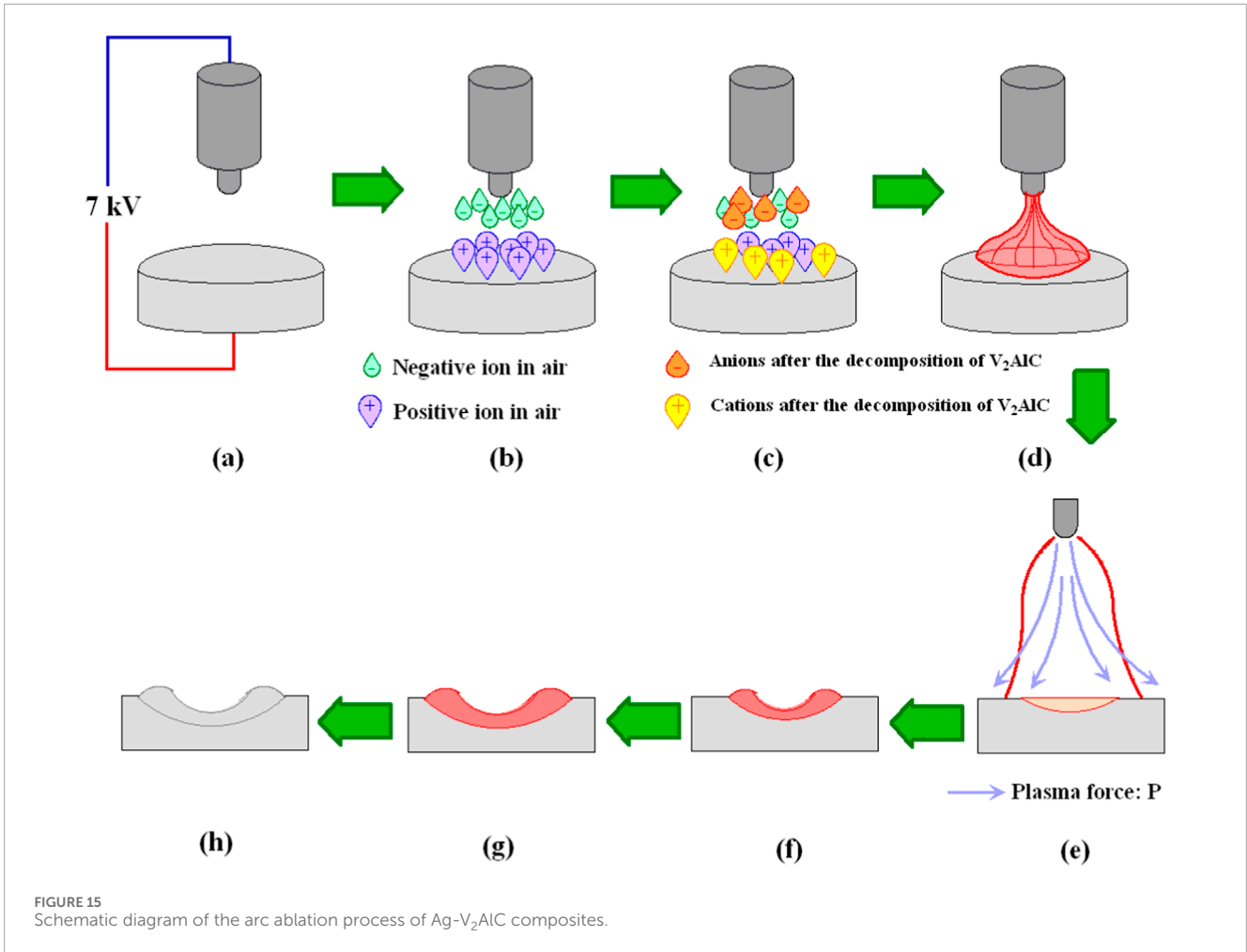

FIGURE 14
Raman spectra of Ag-V$_2$AlC composite ablated by **(a, b)** single arc ablation; **(c)** 10 single arc ablations; **(d)** 100 arc ablations.

breakdown strength (Wang et al., 2010). Therefore, the breakdown strength is related to the preparation process, microstructure of the material, and additives. Metallic silver exhibits a work function of 4.26–4.47 eV (Yang, 1983; Michaelson, 1950), while first-principles calculations predict a significantly higher value (6.4128 eV) for V$_2$AlC. As shown in Figure 4, during single arc ablation, discharges initially localize on the Ag phase due to its lower work function. After 10 discharge cycles, oxide layers (Ag$_2$O, V$_2$O$_5$, Al$_2$O$_3$) form on the Ag-V$_2$AlC surface. These oxides exhibit lower work functions than V$_2$AlC: V$_2$O$_5$: 4.73 eV (Choi et al., 2021), Al$_2$O$_3$: 4.85–5.1 eV (Rajopadhye et al., 1986; Chen et al., 2012) and Ag$_2$O: ~5.0 eV (Wang et al., 2018; Yu et al., 2020; Won Choi et al., 2004). According to the Fowler-Nordheim equation (Koneru et al., 2023; Slade, 2020; Jensen, 2003), arcs preferentially target regions with lower work functions. As oxide layers dominate the surface, they become primary discharge pathways, reducing breakdown strength between the 1st and 14th cycles (Figure 16b). This transition underscores the role of oxide-mediated discharge in progressive material degradation.

(2) Stage II (15–44 discharges): surface roughness evolution and oxide accumulation. To highlight trends in Stages II and III, Figure 16b includes an enlarged inset. During Stage II, the breakdown strength stabilizes between 2.16

× 10^6 V/m and 2.34 × 10^6 V/m—significantly lower than Stage I values. Increased charged particle density in the confined arc chamber lowers the electric field required for positive streamer formation. The extended discharge distance further diminishes breakdown strength. Declining cathode work function due to progressive depletion of the adsorbed gas layer on the Ag-V$_2$AlC surface. Concurrently, oxide layers (Ag$_2$O, V$_2$O$_5$, Al$_2$O$_3$) accumulate, further reducing the composite's effective work function. These combined effects drive the sustained decrease in breakdown strength observed in Stage II.

The surface roughness of the electrode is another critical factor influencing the breakdown strength. Measurements obtained using the software associated with the three-dimensional laser scanning microscope revealed that the surface roughness R$_a$, following 1 and 10 cycles of arc ablation, were 1.584 μm and 5.152 μm, respectively, indicating a significant increase in roughness. The degree of field strength increase can be assessed by the local field enhancement (β) (Huang et al., 2020; Xingang et al., 2015; Kreuger, 1991). These micro-protrusions facilitate strong field emission, and the electric field strength at these locations is considerably higher than the average electric field strength between the two electrodes,

FIGURE 15
Schematic diagram of the arc ablation process of Ag-V$_2$AlC composites.

FIGURE 16
Scatter plots of **(a)** breakdown current and **(b)** breakdown strength with the number of discharges.

making it easier to achieve self-sustained discharge conditions, ultimately leading to a reduction in macroscopic breakdown strength (Pedersen, 1975).

(3) Stage III (45–100 discharges): microstructural modifications. The third stage is slightly lower than the second stage,

fluctuating between 1.7×10^6 V/m and 1.9×10^6 V/m. The content of the generated oxides increases with the number of discharges. This trend accounts for the further decrease in breakdown strength observed in Figure 16 at the third stage, specifically after the number of discharges reaches 47.

Furthermore, after arc ablation, the material's surface develops numerous micro-protrusions, as illustrated in Figures 11, 12. The surface roughness R_a after 100 cycles of arc ablation is 10.153 μm, which is higher than that after 1 and 10 discharges. Previous studies have shown that the electric field can be enhanced by micro-protrusions (Pedersen, 1975). Consequently, the breakdown strength of Ag-V_2AlC composites exhibits a three-stage stepwise decrease following multiple arc ablation.

We fitted the relationship between the 15th to 100th discharges and the change in breakdown strength as shown in Figure 16B. The narrower shaded area is the 95% confidence interval and the wider is the 95% prediction interval, reflecting the range of fluctuations in the data. A polynomial fit was used to fit the second and third stage data points in the figure. As can be seen from the figure, the fitted curves show a high degree of agreement with the original data points, with an overall decreasing trend. The fitting function is y = $2.8682 - 0.02691x + 1.68554 \times 10^{-4} \, x^2$. The Goodness of Fit ($R^2$) is 0.99699.

4 Conclusion

Ag-20 vol.% V_2AlC composites, synthesized via spark plasma sintering (SPS), achieved a relative density of 96.1% and a microhardness of 82.6 HV. The arc ablation mechanisms of these composites (cathode) paired with a tungsten (W) anode were systematically investigated under varying discharge cycles:

(1) Single Discharge: The arc preferentially initiates on the Ag matrix due to its lower work function (4.26–4.47 eV) compared to V_2AlC (6.4128 eV). V_2AlC particles act as pinning sites within the Ag matrix, suppressing material splatter and pore formation. The ablation surface remains flat, with distinct Ag and V_2AlC phases observable. The breakdown strength is 7.9 $\times 10^6$ V/m.

(2) 10 Discharge Cycles: Repeated arc exposure induces a mountain-like morphology at ablation edges, restricting lateral melt pool expansion. Minimal splattering and porosity are observed on the surface. Breakdown strength fluctuates between 4.3×10^6 V/m and 8.2×10^6 V/m.

(3) 100 Discharge Cycles: Oxide formation (V_2O_5, Ag_2O, Al_2O_3) dominates the surface, reducing the effective work function. Micro-protrusions enhance local electric field nonuniformity, further lowering breakdown strength. Additionally, oxide layers increase molten pool viscosity, preventing splattering and porosity despite extensive ablation. Breakdown strength exhibits a three-stage decline. Stage I: 8.24×10^6 V/m → 3.46×10^6 V/m, Stage II: 2.16×10^6 V/m → 2.34×10^6 V/m, Stage III: 1.7×10^6 V/m – 1.9×10^6 V/m.

While this study provides new insights into Ag-MAX composite design, future efforts should focus on:

(1) MAX phase diversity: Systematically compare Ag composites reinforced with Ti_3AlC_2, Ta_2AlC, etc., combined with first-principles calculations to predict their work function and interfacial stability.

(2) Sintering optimization: Evaluate the arc resistance of Ag-MAX composites fabricated via alternative methods.

(3) Multiscale modeling: Develop plasma-molten pool-oxide coupling models to quantify the relationship between MAX phase content and arc energy dissipation.

Data availability statement

The raw data supporting the conclusions of this article will be made available by the authors, without undue reservation.

Author contributions

XH: Funding acquisition, Writing–original draft, Writing–review and editing. JG: Formal Analysis, Funding acquisition, Writing–review and editing. ZZ: Investigation, Methodology, Writing–review and editing. JH: Investigation, Methodology, Writing–review and editing. DZ: Formal Analysis, Methodology, Writing–review and editing. TX: Investigation, Methodology, Writing–review and editing.

Funding

Conflict of interest

The authors declare that the research was conducted in the absence of any commercial or financial relationships that could be construed as a potential conflict of interest.

Generative AI statement

The authors declare that no Generative AI was used in the creation of this manuscript.

Publisher's note

References

Anjum, M., Kumar, R., and Barakat, M. A. (2017). Visible light driven photocatalytic degradation of organic pollutants in wastewater and real sludge using ZnO–ZnS/Ag$_2$O–Ag$_2$S nanocomposite. *J. Taiwan Inst. Chem. Eng.* 77, 227–235. doi:10.1016/j.jtice.2017.05.007

Baddour-Hadjean, R., Smirnov, M. B., Smirnov, K. S., Kazimirov, V. Y., Gallardo-Amores, J. M., Amador, U., et al. (2012). Lattice dynamics of β-V$_2$O$_5$: Raman spectroscopic insight into the atomistic structure of a high-pressure vanadium pentoxide polymorph. *Inorg. Chem.* 51, 3194–3201. doi:10.1021/ic202651b

Barsoum, M. W. (2000). The M$_{N+1}$AX$_N$ phases: a new class of solids: thermodynamically stable nanolaminates. *Prog. Solid State Chem.* 28, 201–281. doi:10.1016/s0079-6786(00)00006-6

Beukema, G. P. (1980). "Electrical breakdown in vacuum," in *Proefschrift rijks universiteit teUtrecht*, 23–53.

Chen, S. Y., Wang, J., Yuan, Z., Wang, Z., and Du, D. (2021). Microstructure and arc erosion behaviors of Ag-CuO contact material prepared by selective laser melting. *J. Alloys Compd.* 860, 158494. doi:10.1016/j.jallcom.2020.158494

Chen, Y. W., Lai, C. M., Cheng, L. W., Hsu, C., and Hsu, C. (2012). Further work function and interface quality improvement on Al$_2$O$_3$ capped high-k/metal gate p-type metal-oxide-semiconductor field-effect-transistors by incorporation of fluorine. *Thin Solid Films* 520, 4482–4485. doi:10.1016/j.tsf.2012.02.087

Choi, S.-G., Seok, H.-J., Rhee, S., Hahm, D., Bae, W. K., and Kim, H. K. (2021). Magnetron-sputtered amorphous V$_2$O$_5$ hole injection layer for high performance quantum dot light-emitting diode. *J. Alloys Compd.* 878, 160303. doi:10.1016/j.jallcom.2021.160303

Ding, K., Ding, J., Zhang, K., Chen, L., Ma, C., Bai, Z., et al. (2022). Micro/nano-mechanical properties evolution and degradation mechanism of Ti$_3$AlC$_2$ ceramic reinforced Ag-based composites under high-temperature arc corrosion. *Ceram. Int.* 48, 33670–33681. doi:10.1016/j.ceramint.2022.07.313

Dong, L. L., Chen, W. G., Deng, N., Song, J., and Wang, J. (2017). Investigation on arc erosion behaviors and mechanism of W70Cu30 electrical contact materials adding graphene. *J. Alloys Compd.* 696, 923–930. doi:10.1016/j.jallcom.2016.12.044

Fu, C. W., Wang, J., Yang, M., Hou, J., and Ding, B. (2012). Microstructure and electrical properties of (Sn$_{0.8}$La$_{0.2}$)O$_2$ coating prepared by plasma spraying. *Acta Metall. Sin.* 49, 325–329. doi:10.3724/SP.J.1037.2012.00599

Gong, Y., and Wang, S. (2025). Effect of V2AlC on the microstructure of copper/graphite composite materials. *Vacuum* 234, 114113. doi:10.1016/j.vacuum.2025.114113

Guzmán, D., González, F., Muranda, D., Aguilar, C., Guzmán, A., Soliz, Á., et al. (2023). Fabrication and Arcrosion behavior of Ag-SnO2-ZnO electrical contact materials. *Materials* 16, 3618. doi:10.3390/ma16103618

Han, T., Li, J., Zhao, N., Shi, C., Liu, E., He, F., et al. (2017). *In-situ* fabrication of nano-sized TiO$_2$ reinforced Cu matrix composites with well-balanced mechanical properties and electrical conductivity. *Powder Technol.* 321, 66–73. doi:10.1016/j.powtec.2017.08.019

Han, Y., Meng, Y., Zhang, C., and Ren, W. (2024). "Wear and corrosion of electrical connectors caused by mechanical operations in high temperature environment," in 2024 IEEE 69th holm conference on electrical contacts (HOLM). Annapolis, MD, USA, 06-10 October 2024 (IEEE), 1–7.

Huang, X., Feng, Y., Qian, G., Zhao, H., Song, Z., Zhang, J., et al. (2018). Arc corrosion behavior of Cu-Ti$_3$AlC$_2$ composites in air atmosphere. *Sci. China-Technological Sci.* 61, 551–557. doi:10.1007/s11431-017-9166-3

Huang, X. C., Feng, Y., Ge, J. L., Li, L., Li, Z., and Ding, M. (2020). Arc erosion mechanism of Ag-Ti$_3$SiC$_2$ material. *J. Alloys Compd.* 817, 152741. doi:10.1016/j.jallcom.2019.152741

Huang, X. C., Feng, Y., Qian, G., and Liu, K. (2017). Erosion behavior of Ti$_3$AlC$_2$ cathode under atmosphere air arc. *J. Alloys Compd.* 727, 419–427. doi:10.1016/j.jallcom.2017.08.188

Huang, X. C., Feng, Y., Qian, G., and Zhou, Z. J. (2019a). Arc ablation properties of Ti$_3$SiC$_2$ material. *Ceram. Int.* 45, 20297–20306. doi:10.1016/j.ceramint.2019.06.305

Huang, X., Feng, Y., Li, L., and Li, Z. (2019b). Erosion behavior of a Cu-Ti$_3$AlC$_2$ cathode by multi-electric arc. *Materials* 12, 1–9. doi:10.3390/ma12182947

Huang, X. C., Li, L., Ge, J. L., Zhao, H., and Zhou, Z. (2024). Investigation on the arc erosion performance of Ag–Ta2AlC composite under air conditions. *J. Adv. Ceram.* 13, 1359–1368. doi:10.26599/jac.2024.9220940

Jensen, K. L. (2003). Electron emission theory and its application: Fowler–Nordheim equation and beyond. *J. Vac. Sci. Technol. B Microelectron. Nanom. Struct. Process. Meas. Phenom.* 21, 1528–1544. doi:10.1116/1.1573664

Jiang, J. W., Fu, C., Yang, M., He, X., Su, X., Ding, B., et al. (2012). Electrical property of nanocomposite Ag/SnO$_2$ electrical contact material prepared by plasma spraying. *Rare Met. Mater Eng.* 41, 1443–1446.

Kesim, M. T., Yu, H., Sun, Y., Aindow, M., and Alpay, S. (2018). Corrosion, oxidation, erosion and performance of Ag/W-based circuit breaker contacts: a review. *Corros. Sci.* 135, 12–34. doi:10.1016/j.corsci.2018.02.010

Koneru, A., Karmarkar, N., Wang, Y., Mohanty, P. S., and Li, B. Q. (2023). Evaluation of cold-sprayed CuCr coatings as contact materials for vacuum interrupters. *Vacuum* 216, 112384. doi:10.1016/j.vacuum.2023.112384

Kreuger, F. H. (1991). *Industrial high voltage*.

Li, H., Cao, Q., Zheng, J., Sun, L., and Rong, W. (2024a). Enhancing the electrical performance of AgNi contact material by doping Ag2WO4. *Mater Lett.* 372, 137009. doi:10.1016/j.matlet.2024.137009

Li, W.-J., Jiang, H., Li, B.-T., Chen, Z. Y., Zhen, L., Jia, S. Y., et al. (2024b). Metallic electrical contact materials: DFT calculations, wetting mechanism and arc resistance. *Mater. Today Phys.* 40, 101333. doi:10.1016/j.mtphys.2024.101333

Ma, Q., Li, Z. R., Niu, H. W., Wang, Z., Ba, J., Qi, J., et al. (2018). The effect of crystal structure of SiO$_2$ on the wettability of AgCuTiSiO$_{2f}$/SiO$_2$ system. *Vacuum* 157, 124–127. doi:10.1016/j.vacuum.2018.08.046

Martína, I., Wiesinger, R., Jembrih-Simbürger, D., and Schreiner, M. (2012). *Micro-Raman characterisation of silver corrosion products: instrumental set up and reference database*.

Michaelson, H. B. (1950). Work functions of the elements. *J. Appl. Phys.* 21, 536–540. doi:10.1063/1.1699702

Mousavi, Z., and Pourabdoli, M. (2022). Physical and chemical properties of Ag–Cu composite electrical contacts prepared by cold-press and sintering of silver-coated copper powder. *Mater Chem. Phys.* 290, 126608. doi:10.1016/j.matchemphys.2022.126608

Nian, Y. H., Zhang, Z. Y., Liu, M. M., and Zhou, X. L. (2023). The electronic structure and stability of Ti$_3$SnC/Ag interface studied by first-principles calculations. *Adv. Theory Simul.* 7, 2300649. doi:10.1002/adts.202300649

Nie, H., Wang, Z., Xue, X., Yu, C., Wang, J., Wen, K., et al. (2024). Designing sandwich-structured Ag–SnO$_2$ contact materials: overcoming the trade-off between erosion resistance and mechanical properties. *Ceram. Int.* 50, 2950–2962. doi:10.1016/j.ceramint.2023.11.040

Nie, Y., Liu, J., Ke, J., Zhao, X., Li, S., and Zhu, Y. (2023). Investigation on AC and DC breakdown mechanism of surface-ozone-treated LDPE films under varied thicknesses. *Polymers* 15, 4490. doi:10.3390/polym15234490

Pedersen, A. (1975). The effect of surface roughness on breakdown in SF$_6$. *IEEE Trans. Power Apparatus Syst.* 94, 1749–1754. doi:10.1109/t-pas.1975.32019

Rajopadhye, N. R., Dake, S. B., and Bhoraskar, S. V. (1986). Characterization of Al$_2$O$_3$ films deposited by various methods. *Thin Solid Films* 142, 127–138. doi:10.1016/0040-6090(86)90308-1

Slade, P. G. (2020). *The vacuum interrupter: theory, design, and application*. Boca Raton: CRC.

Smirnov, M. B., Roginskii, E. M., Smirnov, K. S., Baddour-Hadjean, R., and Pereira-Ramos, J. P. (2018). Unraveling the structure–Raman spectra relationships in V$_2$O$_5$ polymorphs via a comprehensive experimental and DFT study. *Inorg. Chem.* 57, 9190–9204. doi:10.1021/acs.inorgchem.8b01212

Sone, H., and Takagi, T. (1990). Role of the metallic phase arc discharge on arc erosion in Ag contacts. *IEEE Trans. Compon. Hybrids Manuf. Technol.* 13, 13–19. doi:10.1109/33.52844

Sun, Z. M. (2011). Progress in research and development on MAX phases: a family of layered ternary compounds. *Int. Mater Rev.* 56, 143–166. doi:10.1179/1743280410y.0000000001

Wang, C.-T., Ting, C.-C., Kao, P.-C., Li, S. R., and Chu, S. Y. (2018). Improvement of OLED performance by tuning of silver oxide buffer layer composition on silver grid surface using UV-ozone treatment. *Appl. Phys. Lett.* 113, 051602. doi:10.1063/1.5043141

Wang, D., Tian, W., Ding, J., Zhu, Y., Zhang, P., Zhang, Y., et al. (2020). The beauty and the deed of silver during arc erosion of Ag/Ti$_3$AlC$_2$ contacts. *J. Alloys Compd.* 820, 153136. doi:10.1016/j.jallcom.2019.153136

Wang, D., Tian, W., Ma, A., Ding, J., Wang, C., You, Y., et al. (2019a). Anisotropic properties of Ag/Ti$_3$AlC$_2$ electrical contact materials prepared by equal channel angular pressing. *J. Alloys Compd.* 784, 431–438. doi:10.1016/j.jallcom.2019.01.083

Wang, D., Xia, Z., Lu, C., Wang, J., Zhu, H., Hu, J., et al. (2024). Effect of M-site element on the interaction of M2AlC and Ag and the induced properties of Ag/M2AlC composites. *J. Mater. Res. Technol.* 31, 870–878. doi:10.1016/j.jmrt.2024.06.133

Wang, H., Liu, W., Yang, M., and Zhu, Y. (2022). Effect of particle size of second phase on wettability and electrical contact properties of AgSnO$_2$ contact materials. *Rare Met. Mater Eng.* 51, 24–29.

Wang, H., Wang, Y., Wang, J., Cai, Q., and Hu, D. (2023a). Enhancement of arc erosion resistance in AgCuO electrical contact materials through rare earth element doping: first-principles and experimental studies. *Int. J. Mol. Sci.* 24, 12627. doi:10.3390/ijms241612627

Wang, J., Duan, C., Chen, S., Hu, H., Zhang, Q., Chang, Y., et al. (2023b). Arc erosion behaviors and surface characteristics of SnO_2 nanofiber/particle reinforced Ag-based composite. *J. Mater Eng. Perform.* 33, 4754–4764. doi:10.1007/s11665-023-08300-x

Wang, J., Zhao, H., Wang, J., Fu, C., and Chang, Y. (2019b). Effect of CuO additives on the formation of SnO_2-rich layers in Ag-SnO_2 materials. *J. Alloys Compd.* 770, 920–925. doi:10.1016/j.jallcom.2018.08.159

Wang, X., Liang, S., Yang, P., and Fan, Z. (2010). Effect of Al2O3 content on electrical breakdown properties of Al2O3/Cu composite. *J. Mater Eng. Perform.* 19, 1330–1336. doi:10.1007/s11665-010-9607-3

Won Choi, H., Young Kim, S., Kim, K.-B., Tak, Y. H., and Lee, J. L. (2004). Enhancement of hole injection using O_2 plasma-treated Ag anode for top-emitting organic light-emitting diodes. *Appl. Phys. Lett.* 86, 012104. doi:10.1063/1.1846149

Wu, C., Wu, X., Ding, J., Ding, K., Zhang, P., Ma, C., et al. (2025). Achieving highly conductive Ag/Ti3AlC2 composite by inhibiting interdiffusion. *Scr. Mater* 255, 116343. doi:10.1016/j.scriptamat.2024.116343

Wu, X. L., Wu, C. Z., Wei, X. P., Sun, W., Zhang, Y., et al. (2024). Influence of nano-mechanical evolution of Ti_3AlC_2 ceramic on the arc erosion resistance of Ag-based composite electrical contact material. *J. Adv. Ceram.* 13, 176–188. doi:10.26599/jac.2024.9220839

Xiao, X, Fan, Z., Liang, S., and Xiao, P. (2007). Effects of TiC on microstructures and properties of CuW electrical contact materials. *Rare Met. Mater Eng.* 36, 817–821.

Xingang, W., Zhang, H., Li, W., Liu, L., Shi, B., and Yang, Z. (2015). Effect of preparation process on microstructure and arc-erosion resistance of WCu30 Alloy. *Rare Met. Mater Eng.* 44.

Yang, J. J. (1983). *Gas discharge*. Beijng: Science Press, 52.

Yang, X., Sheng, J., Zhao, Y., Li, L., Xiao, P., and Liang, S. (2024). Effect of TiB2 on properties and microstructures of CuW electrical contact materials. *Int. J. Refract Met. Hard Mater* 119, 106542. doi:10.1016/j.ijrmhm.2023.106542

Yu, H.-L., Wu, Q.-X., Wang, J., Liu, L. Q., Zheng, B., Zhang, C., et al. (2020). Simple fabrication of the Ag-Ag_2O-TiO_2 photocatalyst thin films on polyester fabrics by magnetron sputtering and its photocatalytic activity. *Appl. Surf. Sci.* 503, 144075. doi:10.1016/j.apsusc.2019.144075

Zhao, J., Li, H., Xie, M., Chen, Y., Nie, B., and Bi, Y. (2024). Electrical contact behavior of Ag-SnO_2-In_2O_3 contact materials prepared via pressurized powder internal oxidation. *Mater. Today Commun.* 38, 108357. doi:10.1016/j.mtcomm.2024.108357

Zhao, J., Xie, M., and Li, H. (2023). Low-temperature sintering and infiltration of high-W contacts. *Appl. Sci.* 13, 9608. doi:10.3390/app13179608

Zhou, K., Chen, W., Feng, P., Yan, F., and Fu, Y. (2020). Arc ablation behavior and microstructure evolution of plastically deformed and micro-alloyed Cu–Cr–Zr alloys. *J. Alloys Compd.* 820, 153123. doi:10.1016/j.jallcom.2019.153123